## PHYSICS

# Ultrahigh dielectric permittivity in oxide ceramics by hydrogenation

Nguyen Xuan Duong[1], Ji-Soo Jang[2], Min-Hyoung Jung[3], Jong-Seong Bae[4], Chang Won Ahn[1], Jong Sung Jin[4], Kyuwook Ihm[5], Gyehyeon Kim[6], So Yeon Lim[7], Jongmin Lee[8], Dang Duc Dung[9], Soonil Lee[10], Young-Min Kim[3], Sanghan Lee[8], Sang Mo Yang[11], Changhee Sohn[6], Ill Won Kim[1], Hu Young Jeong[12], Seung-Hyub Baek[2], Tae Heon Kim[1]*

Boosting dielectric permittivity representing electrical polarizability of dielectric materials has been considered a keystone for achieving scientific breakthroughs as well as technological advances in various multifunctional devices. Here, we demonstrate sizable enhancements of low-frequency dielectric responses in oxygen-deficient oxide ceramics through specific treatments under humid environments. Ultrahigh dielectric permittivity ($\sim 5.2 \times 10^6$ at 1 Hz) is achieved by hydrogenation, when Ni-substituted BaTiO$_3$ ceramics are exposed to high humidity. Intriguingly, thermal annealing can restore the dielectric on-state (exhibiting huge polarizability in the treated ceramics) to the initial dielectric off-state (displaying low polarizability of $\sim 10^3$ in the pristine ceramics after sintering). The conversion between these two dielectric states via the ambient environment–mediated treatments and the successive application of external stimuli allows us to realize reversible control of dielectric relaxation characteristics in oxide ceramics. Conceptually, our findings are of practical interest for applications to highly efficient dielectric-based humidity sensors.

## INTRODUCTION

Up to now, dielectric materials with ultrahigh electrical polarizability (i.e., dielectric permittivity) have been in enormous demand for potential applications to a large variety of functional devices such as field-effect transistors (1), dynamic random access memories (2), high–energy-density storage (3), and passive sensors (4, 5). It has been known that a huge dielectric constant ($\sim 8000$ for perovskite BaTiO$_3$) in conventional ferroelectrics has been produced at the Curie temperature ($T_C$) where a dielectric anomaly appears with a ferroelectric-to-paraelectric phase transition (6, 7). Such a high dielectric constant has been only achieved in the limited range of temperature around $T_C$ ($\sim 120°C$), which would not be suitable for applications to actual devices operating at room temperature (8, 9). Note that the large dielectric permittivity in bulk BaTiO$_3$ has been accessible with a finite value in the frequency range from $10^2$ to $10^6$ Hz as well (10). To overcome these limitations in the device applications, numerous studies on dielectric dispersion characteristics in dielectrics have been fulfilled for several material systems including double perovskite oxides (11, 12), TiO$_2$ (13, 14), and doped/undoped BaTiO$_3$ (15, 16). Colossal dielectric permittivity in complex oxide CaCu$_4$Ti$_4$O$_{12}$ ceramics has been previously reported with a maximum dielectric constant of $\sim 10^5$ (approximately an order of magnitude larger than the dielectric constant of pure BaTiO$_3$) over a wide range of temperature from 100 to 600 K exhibiting better thermal stability (17–19). It should be also noted that the giant dielectric permittivity has been strongly dependent on ac frequency in the frequency domain of $10^1$ to $10^6$ Hz (17, 20). Despite the fascinating earlier work of unusual dielectric properties in oxide materials, a microscopic origin of the colossal dielectric permittivity is still under debate and remains unclear (13, 21, 22).

In a technological point of view, exceptionally large dielectric permittivity, which can be manipulated by external stimuli, is of practical interest for applications of functional oxides to sensing devices with high performance (23–25). In a common sensing principle, the sensing capability (i.e., sensitivity) of gas sensors has been estimated to the variation of electrical properties (e.g., electrical current, resistance, and capacitance) under a gas environment with respect to a reference situation (26, 27). For example, in a capacitive type of sensor, one of the most popular classes of commercial gas sensors (28, 29), the sensitivity ($S$) has been determined by a relative change of capacitance under an ambient atmosphere as follows (30–32)

$$S\,(\%) = \frac{C_g - C_o}{C_o} \times 100 \tag{1}$$

where $C_g$ and $C_o$ represent the capacitances of a sensor in the gas circumstance and the reference condition, respectively. Considering that a capacitance in lossy dielectrics is usually coupled with electrical conductivity (33, 34), a change of the capacitance (proportional to dielectric permittivity) would be monitored by a variation in the resistance. Hence, to realize dielectric-based gas sensors with enhanced sensitivity, a difference in the dielectric permittivity

[1]Department of Physics and Energy Harvest-Storage Research Center (EHSRC), University of Ulsan, Ulsan 44610, Republic of Korea. [2]Electronic Materials Research Center, Korea Institute of Science and Technology, Seoul 02792, Republic of Korea. [3]Department of Energy Science, Sungkyunkwan University (SKKU), Suwon 16419, Republic of Korea. [4]Busan Center, Korea Basic Science Institute (KBSI), Busan 46742, Republic of Korea. [5]Pohang Accelerator Laboratory, Pohang 37673, Republic of Korea. [6]Department of Physics, Ulsan National Institute of Science and Technology (UNIST), Ulsan 44919, Republic of Korea. [7]Department of Physics, Sookmyung Women's University, Seoul 04310, Republic of Korea. [8]School of Materials Science and Engineering, Gwangju Institute of Science and Technology, Gwangju 61005, Republic of Korea. [9]School of Engineering Physics, Ha Noi University of Science and Technology, 1 Dai Co Viet Road, Ha Noi, Viet Nam. [10]School of Materials Science and Engineering, Changwon National University, Changwon 51140, Republic of Korea. [11]Department of Physics, Sogang University, Seoul 04107, Republic of Korea. [12]Graduate School of Semiconductor Materials and Devices Engineering, Ulsan National Institute of Science and Technology (UNIST), Ulsan 44919, Republic of Korea.
*Corresponding author. Email: thkim79@ulsan.ac.kr

between the treated (surrounded by an ambient gas) and pristine states should be boosted further.

Hydrogenation is a promising way for promoting dielectric properties in oxide materials and, thereby, for achieving high-efficient sensing devices like a hygrometer. Very recently, notable advances have been accomplished to tailor a substantial extent of physical properties of functional oxides via protonation (35–37). The pioneering work clearly demonstrated that the crystal and electronic structures (35, 36) and the electrical, magnetic, and transport characteristics (35, 37) have been reversibly controllable by implementing protonation and deprotonation processes alternately. We note that a hydrogen ion (i.e., $H^+$) is electrically positive and highly mobile because of both the lightest ionic mass and the smallest ionic radius (38, 39). Hence, the hydrogen ion can generate an electric field locally, when it is introduced into complex oxide compounds (40, 41). For dielectric materials, it is highly plausible that a lattice structure at the given site incorporating a proton is deformed with polarization induced by a local internal field accompanying a modification of the associated physical properties (40, 41). However, the detailed studies of dielectric responses to hydrogenation in complex oxides have been extremely rare up to our knowledge. A systematic approach is highly essential to figure out the hydrogenation effect on dielectric properties technologically and scientifically.

Hexagonal $BaTiO_3$ is an excellent platform for examining the modification of dielectric properties induced by hydrogenation in dielectric materials (42). The nonperovskite $BaTiO_3$ polymorph with a 6H-hexagonal structure (h-$BaTiO_3$, $P6_3/mmc$) is energetically stable at a high temperature (>1460°C) for the stoichiometric composition (42, 43). Very recently, it has been experimentally reported that the hexagonal $BaTiO_3$ phase can be stabilized at room temperature by doping of transition-metal ions into undoped $BaTiO_3$, resulting in the formation of non-neutral ionic defects (i.e., cation and oxygen vacancy defects) (44–46). In particular, in the presence of oxygen vacancy ($V_O^{\bullet\bullet}$) defects induced by cation acceptor doping and/or substitution, the polar Ti-O hybridization in the perovskite $BaTiO_3$ is weakened, enabling the realization of the hexagonal polymorph (45–47). At the oxygen vacancy sites, it is energetically favorable for gas molecules from ambient environments to be adsorbed on the surface of complex oxides (41, 48). In our case, while a hydroxyl ion ($OH^-$) dissociated from a water molecule in air is adsorbed on the surface oxygen vacancies with a positive ionic charge in hexagonal $BaTiO_3$, the split hydrogen ion ($H^+$) would be introduced to the oxygen-deficient $BaTiO_3$ because of its high mobility (49). Note that the non-neutral ionic charges (e.g., protons) should easily migrate by application of an electric field (50). Moreover, dielectric relaxation behaviors in the low-frequency range are very sensitive to the spatial distribution of mobile ionic charges (15, 34, 51), and thereby, it is possible for us to tailor the dielectric permittivity/loss in doped/substituted $BaTiO_3$ through hydrogenation.

In this work, we systematically examined how the dielectric characteristics in oxide ceramics evolved depending on ambient conditions. To achieve our aim, we synthesized oxygen-deficient 6H-hexagonal $BaTiO_3$ ceramics with Ni substitution and monitored their dielectric responses to various ambient environments. We
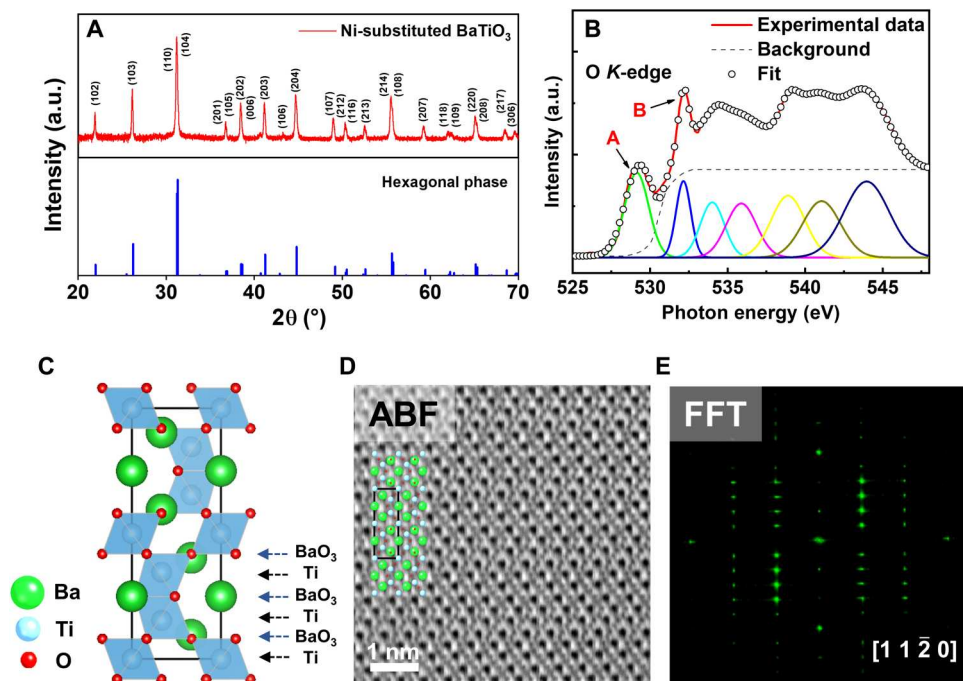


**Fig. 1. Crystal and electronic structures in the as-sintered Ni-substituted BaTiO₃ ceramics.** (A) XRD pattern of the as-sintered Ni-substituted $BaTiO_3$ ceramics at a doping concentration $x = 0.175$. a.u., arbitrary units. (B) The normalized O $K$-edge x-ray absorption spectra of the Ni-substituted $BaTiO_3$ ceramics. Peaks A and B were respectively attributed to the transition from O $1s$ to $t_{2g}$ and $e_g$ hybridized states between O $2p$–Ti $3d$. (C) Schematic diagram of the hexagonal $BaTiO_3$ structure viewed along the [11$\overline{2}$0] direction. (D) ABF-STEM images of the as-sintered Ni-substituted $BaTiO_3$ ceramic along [11$\overline{2}$0] zone axis. The projected lattice structure of the hexagonal phase was superimposed in (D). The green, blue, and red balls represented the Ba, Ti, and O atoms, respectively. (E) The corresponding fast Fourier transform (FFT) pattern of the Ni-substituted $BaTiO_3$ ceramic along the [11$\overline{2}$0] zone axis.

found that the frequency-dependent dielectric relaxation behaviors were quite sensitive to moisture in air. In the humidity-exposed Ni-substituted BaTiO₃ ceramics, we observed a notable increase in the low-frequency dielectric permittivity at room temperature, whereas there was no dielectric anomaly in the as-sintered ceramics. The dielectric constant in the low-frequency region was three orders of magnitude higher (~$10^6$ at 1 Hz; the on-state) in the treated ceramics under water vapor–rich situations than that (~$10^3$ at 1 Hz; the off-state) in the as-sintered ceramics. We identified that these two dielectric states were reversible through specific treatments under ambient conditions and subsequent external stimulation. The introduction of hydrogen ions dissociated from water molecules to oxygen-deficient BaTiO₃ ceramics and thereby spatial inhomogeneity of electrical polarizability by hydrogenation would produce a sizable enhancement (i.e., the on-state) of dielectric permittivity on a macroscopic scale. By harnessing such two dielectric states alternately tunable by external stress, we also demonstrated potential applications to actual gas sensors such as a hygrometer.

## RESULTS

The crystal and electronic structures of the as-sintered Ni-substituted BaTiO₃ [Ba(Ti$_{1-x}$Ni$_x$)O$_{3-\delta}$, $x = 0.175$] were characterized by x-ray diffraction (XRD), x-ray absorption spectroscopy (XAS), and scanning transmission electron microscopy (STEM), as shown in Fig. 1. It was clear that the XRD θ-2θ spectra (solid red lines in Fig. 1A) of the Ni-substituted BaTiO₃ ceramics were well matched with the reference XRD pattern (marked by the blue bar in Fig. 1A) of hexagonal BaTiO₃, indicative of the formation of a hexagonal polymorphic phase by Ni substitution (45, 46). We accentuate that oxygen vacancies in heavily substituted BaTiO₃ ceramics play a crucial role in stabilizing the hexagonal polymorph at room temperature (42, 46). XAS revealed that the absorption peak (denoted by "A" in Fig. 1B) of a transition from O 1s to Ti 3d $t_{2g}$ orbitals in O 2p–Ti 3d hybridization was markedly suppressed in the Ni-substituted BaTiO₃ compared with pure BaTiO₃ ceramics (see fig. S1). In contrast, there was little variation in the peak intensity (denoted by "B" in Fig. 1B) of a transition from O 1s to Ti 3d $e_g$ orbitals between the Ni-substituted and pure BaTiO₃ ceramics. Considering that the intensity of the absorption peak A is susceptible to oxygen off-stoichiometry in complex oxides (52, 53), our Ni-substituted BaTiO₃ ceramics should incorporate a larger amount of oxygen vacancies than pure BaTiO₃ ceramics, allowing us to realize the hexagonal phase in the oxygen-deficient substituted BaTiO₃.

Annular bright-field (ABF)–STEM analyses showed that the as-sintered Ni-substituted BaTiO₃ ceramics were structurally 6H-hexagonal following the hexagonal close-packing scheme of ABCACB in a single unit cell, as depicted in Fig. 1C (42, 43, 54). In the lattice structure of the 6H-hexagonal BaTiO₃, the BaO₃ and Ti sublayers are alternatively stacked in the [0001] direction, and two pairs of face-sharing TiO₆ octahedra are interconnected through a corner-sharing TiO₆ octahedron (42–44). The ABF-STEM images along the [11$\bar{2}$0] zone axis indicated that the atomic stacking sequence of the BaO₃ and Ti sublayers is quite consistent with the stacking order of the projected lattice structure of the 6H-hexagonal BaTiO₃ along the [11$\bar{2}$0] direction (Fig. 1D). We also identified that six BaO₃ layers were vertically piled up in accordance with the hexagonal close-packed arrangement (ABCACB). From the

fast Fourier transform pattern obtained from the STEM images (Fig. 1E), we also found that the diffraction spots are well indexed by the simulated electron diffraction peaks of a 6H-hexagonal structure along the [11$\bar{2}$0] zone axis (fig. S2).

To examine how dielectric responses of substituted BaTiO₃ compounds evolve in air over time, we performed a series of experimental measurements for the as-sintered Ni-substituted BaTiO₃ ceramics, as shown in Fig. 2A. At room temperature, we first measured dielectric permittivity (ε) (marked by the red circle) in the frequency range from $10^0$ to $10^5$ Hz and polarization-electric field (P-E) hysteretic characteristics (marked by the green circle). The subsequent experiment was also carried out to quantify the temperature-dependent dielectric constant (marked by the blue circle) with increasing temperature (from 30° to 350°C). To assess an effect of the ambient air on the dielectric properties of the Ni-substituted BaTiO₃ compounds, the ceramic samples remained in air at room temperature for the time duration of 6 weeks, and thereafter, the corresponding dielectric responses were repeatedly characterized for identical specimens using the same experimental manner. For the as-sintered state, a low dielectric constant of ~$10^3$ was observed throughout the whole frequency range with slight variations (Fig. 2B). The polarization responses to the external electric fields were very linear with small hysteresis (Fig. 2C), which is characteristic of conventional dielectric materials with little electrical leakage (34). We also note that linear P-E curves were previously reported in substituted BaTiO₃ ceramics with 6H-hexagonal symmetry (45, 55). In the temperature-dependent dielectric data of the as-sintered ceramics (Fig. 2D), there was no noticeable anomaly in the dielectric permittivity at all temperatures. Accordingly, we named the as-sintered state of our Ni-substituted BaTiO₃ ceramics as an "off-state."

After Ni-substituted BaTiO₃ ceramics were exposed to air at room temperature for 6 weeks, it was quite intriguing that the dielectric properties of the treated ceramics became completely different from those of the as-sintered ceramics. As shown in Fig. 2E, it was evident that the treated Ni-substituted BaTiO₃ ceramics exhibited dielectric relaxation behaviors as frequency increased. The low-frequency dielectric constant at 1 Hz increased up to ~$4.6 \times 10^4$, and it gradually decreased with increasing frequency. The P-E hysteresis curve with an elliptical shape was observed in the treated ceramics (Fig. 2F). Considering that leakage currents largely contributed to the open P-E hysteresis in lossy dielectrics (56), it is highly likely that our Ni-substituted BaTiO₃ ceramics became electrically leaky after the 6 weeks of air exposure. A broad/smooth dielectric transition clearly appeared in the temperature range of 30° to 190°C (Fig. 2G). In the temperature dependence of dielectric permittivity, it was evident that the dielectric anomaly was more pronounced with decreasing frequency. At frequencies of $10^3$, $10^4$, and $10^5$ Hz, the maximum values of dielectric permittivity (ε) were estimated to be ~$1.1 \times 10^4$, $5.1 \times 10^3$, and $1.0 \times 10^3$ in the vicinity of the transition temperature, respectively. Such an ultrahigh dielectric constant (named as an "on-state") in the treated states of our Ni-substituted BaTiO₃ ceramics was reminiscent of earlier results of colossal dielectric permittivity observed in the temperature-dependent dielectric dispersions of various oxide ceramics (57, 58). It is also worthwhile to note that there was no difference in the frequency-dependent dielectric permittivity data of pure BaTiO₃ ceramics with tetragonal symmetry, although the pure BaTiO₃ ceramics were treated via the 6-week-durational air exposure (fig. S3). For
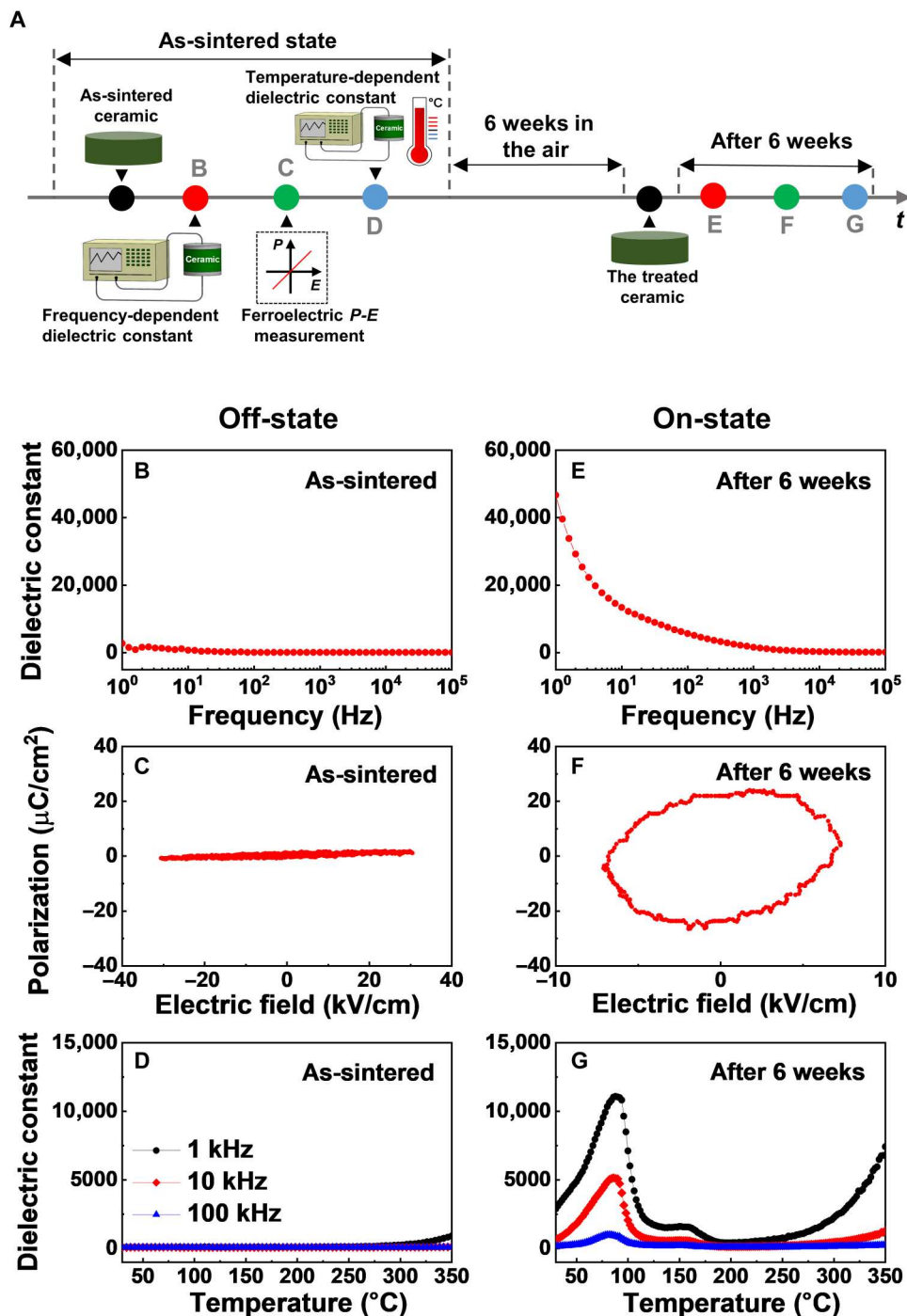
**Fig. 2. The change of dielectric responses in Ni-substituted BaTiO₃ ceramics under the ambient air environment.** (**A**) A schematic diagram of the experimental sequence. Red, green, and blue circles represented frequency-dependent dielectric constant at room temperature, polarization-electric field hysteresis loop, and temperature-dependent dielectric constant measurements, respectively. (**B**) The frequency dependence of permittivity, (**C**) the *P-E* loop, and (**D**) the temperature-dependent dielectric constant in the as-sintered Ni-substituted BaTiO₃ ceramics. We exposed the as-sintered ceramics to the ambient air and then remeasured the dielectric properties after a time duration of 6 weeks. (**E**) The frequency-dependent dielectric constant, (**F**) the hysteresis loop, and (**G**) the temperature dependence of dielectric permittivity in the treated ceramic samples.

both the as-sintered and treated states, a slight upturn behavior (i.e., the dielectric constant at 1 Hz increased up to ~$10^4$) only appeared in the low-frequency region due to the room temperature ferroelectricity.

To check whether these two dielectric states (i.e., off- and on-states for the as-sintered and treated samples, respectively) can be manipulated by external stimuli, we thermally annealed the Ni-substituted BaTiO$_3$ ceramics that had been treated by air exposure for 6 weeks. The treated sample was heated in a muffle furnace at 350°C for 1 hour under ambient air environment, as schematically displayed in Fig. 3A. Then, we repeated the measurements of frequency-dependent dielectric constant (indicated by the red circle), the polarization-electric field (P-E) hysteresis (indicated by the green circle), and the temperature-dependent permittivity (indicated by the blue circle) in the annealed Ni-substituted BaTiO$_3$ ceramics. Unexpectedly, the huge dielectric permittivity (i.e., the on-state) of the treated ceramics in the low-frequency region totally vanished in the annealed ceramics (Fig. 3B). After the heat treatment, the resulting P-E curve became linear with little hysteresis as well (Fig. 3C). In the temperature-dependent dielectric dispersions of the annealed ceramic sample, it was clear that dielectric anomalies observed in the treated ceramic sample were quite suppressed with no distinct transition around 30° to 190°C (Fig. 3D). Namely, the on-state in the treated sample by air exposure was restored to the initial off-state in the as-sintered sample by thermal annealing. This indicated that the on-state exhibiting ultrahigh dielectric permittivity at low frequencies was turned off in our Ni-substituted BaTiO$_3$ ceramics via a thermally assisted reset process. It was further interesting that such resetting of the on-state to the off-state in dielectric responses was feasible by applying electric dc bias to the treated ceramic specimens representing the dielectric on-state (fig. S4 and table S1).

To identify the tunability between the off- and on-states in Ni-substituted BaTiO$_3$ ceramics, we exposed the annealed ceramic samples to air at room temperature for 6 weeks once again and then remeasured all the dielectric properties of the retreated ceramic samples (marked by the red, green, and blue circles in Fig. 3A). It was explicit that the suppressed dielectric responses (i.e., the off-state) in the low-frequency region were recovered in the retreated ceramics representing an extremely large dielectric permittivity (ε ~ 6.9 × $10^4$ at 1 Hz) in the frequency-dependent dielectric constant data (Fig. 3E). In addition, the P-E loop (Fig. 3F) and the temperature-dependent dielectric behaviors (Fig. 3G) in the off-state returned to the characteristics of the on-state. The reversible changes of low-frequency dielectric permittivity were clearly demonstrated by systematically monitoring the frequency dependence of dielectric responses as a function of the duration time for the as-sintered and annealed states (see fig. S5). Here, the frequency-dependent dielectric relaxation behaviors of the as-sintered and annealed Ni-substituted BaTiO$_3$ ceramics have been tracked every week. Over time, the dielectric constants corresponding to low frequencies progressively increased beyond 1 to 2 weeks after the sintering and annealing processes, as shown in fig. S5 (D and G), respectively. It was therefore possible that these off- and on-states in the dielectric properties of our Ni-substituted BaTiO$_3$ ceramics were reversibly controllable through specific treatments under chemical environments (e.g., exposure to ambient air) and external stimulation (e.g., application of heat and electric fields).

To observe the evolution of dielectric responses to ambient environments in Ni-substituted BaTiO$_3$ ceramics, we constructed several experiments (for more details, see Materials and Methods). Here, the frequency-dependent dielectric constant (Fig. 4A) and loss (Fig. 4B) were repetitively measured before (indicated by the black solid squares) and after (indicated by the red solid circles) implementing various atmosphere treatments (i.e., air, vacuum, N$_2$ gas, CO$_2$ gas, and high humidity) for the as-sintered Ni-substituted BaTiO$_3$ ceramics for a particular time duration. To secure the experimental reliability, a desiccator was vacuumed to the base pressure of ~380 torr before all ambient treatments (fig. S6 and table S2). Except for a situation surrounding high humidity, there was seemingly no difference in the frequency-dependent dielectric constant, when the as-sintered ceramic samples were exposed to air, vacuum, N$_2$, and CO$_2$ environments for 1 week. The measured dielectric permittivity was quite low with a constant value of ~$10^3$ in the whole frequency range, while a little change in the frequency-dependent dielectric loss was observed after the ambient treatments. This indicated that the initial off-state in the as-sintered Ni-substituted BaTiO$_3$ ceramics was not affected by the exposure to air, vacuum, N$_2$, and CO$_2$ circumstances. It was also plausible that the ceramic samples exposed to these ambient conditions still remained in the off-state with no change in dielectric permittivity.

A modification of dielectric permittivity in our Ni-substituted BaTiO$_3$ ceramics induced by air exposure was closely associated with the presence of water molecules in ambient air. We identified substantial changes in the dielectric responses of as-sintered ceramics, when the ceramic samples were treated under a highly humid condition for 2 days simply (Fig. 4, bottom). The treated Ni-substituted BaTiO$_3$ under the high-humidity situation incorporating abundant moistures exhibited three orders of magnitude higher dielectric constant (ε ~ 5.2 × $10^6$; the on-state) at 1 Hz than the as-sintered Ni-substituted BaTiO$_3$ (ε ~ $10^3$; the off-state) (Fig. 4A, bottom). Such a giant dielectric constant in the treated Ni-substituted BaTiO$_3$ ceramics was comparable to the reported values of colossal dielectric permittivity ($10^6$ to $10^7$) in the low-frequency region elsewhere (for more details, see table S3). After the high-humidity treatment, the corresponding dielectric loss also increased up to the measurement limit (tanδ ~ 10) (Fig. 4B, bottom). It should be also noted that the time duration (2 days) for the ambient treatment under a humid environment is even shorter than that (1 week) for other treatments.

Such a change in dielectric responses driven by moisture was reversible, and hence, the on-state in the treated sample by humidity could go back to the off-state in the pristine (i.e., as-sintered) sample through either thermal annealing (Fig. 5) or electrical dc biasing (fig. S4 and table S1). Furthermore, the ambient environment–induced modification of dielectric properties (i.e., a transformation from the off-state to the on-state) in Ni-substituted BaTiO$_3$ ceramics was achievable by directly immersing the as-sintered ceramic samples in distilled water for a very short time duration (~10 min) (fig. S7). We also stress that such a dielectric phase transition by the water treatment was only attainable in the Ni-substituted BaTiO$_3$ with oxygen deficiency, not pure BaTiO$_3$ ceramics (fig. S7, D and E). Accordingly, water molecules in air play a critical role in producing ultrahigh dielectric permittivity (in the low-frequency range of $10^0$ to $10^2$ Hz) in our Ni-substituted BaTiO$_3$ ceramics.
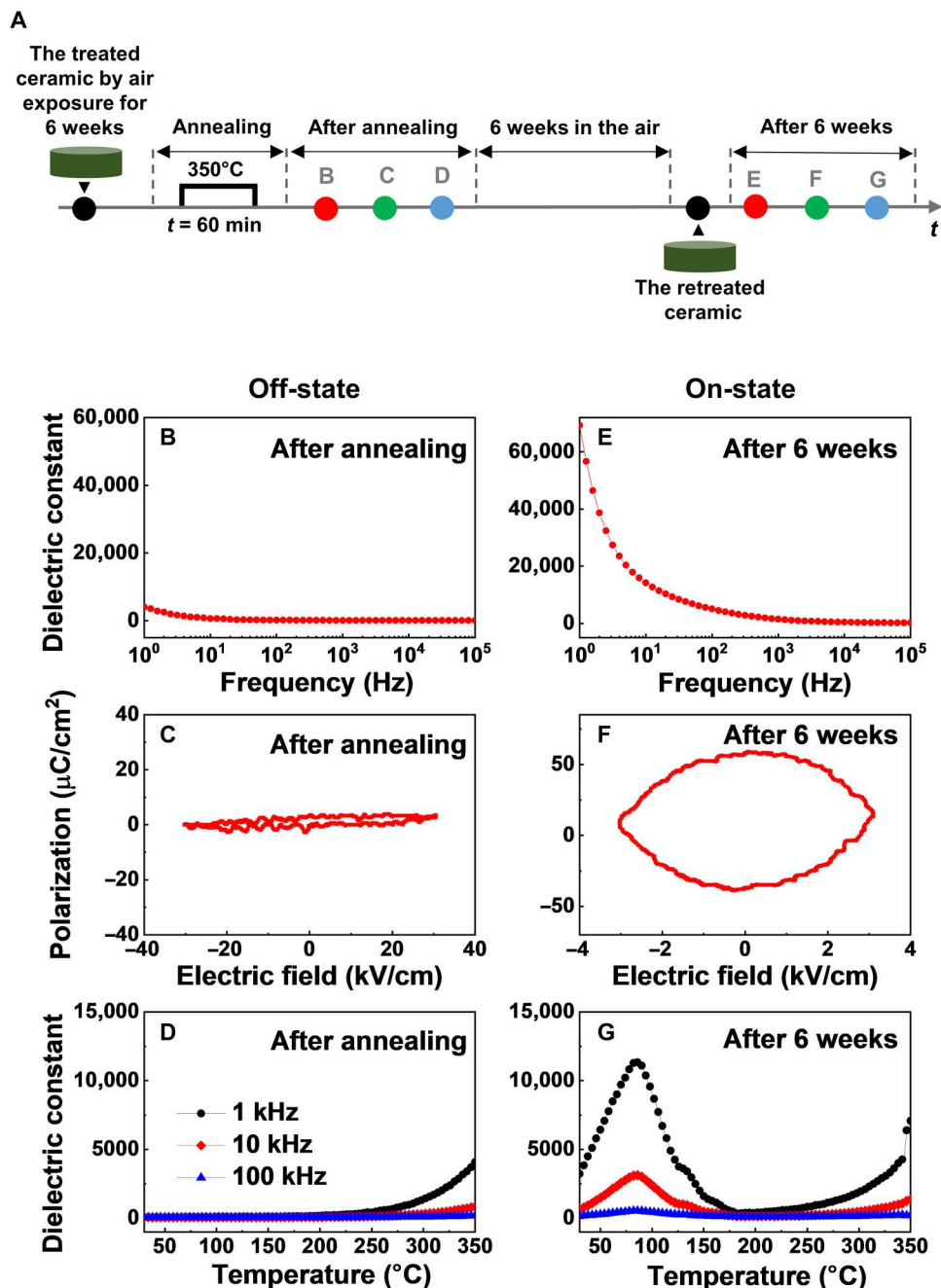
**Fig. 3. The reversible change of the dielectric responses in BaTiO₃ ceramics through thermal annealing and air exposure.** (**A**) A schematic figure of the experimental sequence. The treated Ni-substituted BaTiO₃ ceramics by air exposure were annealed at 350°C for 1 hour. (**B**) The frequency-dependent dielectric constant in treated ceramics after thermal annealing. (**C**) The hysteresis loop of annealed ceramic samples. (**D**) The temperature dependence of dielectric constant of the annealed Ni-substituted BaTiO₃ ceramics. The annealed ceramics were treated via air exposure for 6 weeks. (**E**) The frequency-dependent dielectric constant, (**F**) the *P-E* hysteresis loop, and (**G**) the temperature-dependent dielectric behavior in retreated ceramics by ambient air environment.

To examine how stable the reversible change between two different dielectric states was in our Ni-substituted BaTiO₃ ceramics, we repeated a cycle of specific treatment under a humid environment and subsequent thermal annealing five times (for more details, see Fig. 5A and Materials and Methods). As shown in Fig. 5B, it was clear that the resulting dielectric on- and off-states alternately appeared over 5 cycles of the high-humidity treatment and the thermal annealing. The frequency-dependent dielectric relaxation behaviors of the on- and off-states were also reproducible every cycle. In addition, the dielectric constants (at 1 Hz) between the on- and off-states were tracked and plotted as a function of the number of cycle (Fig. 5C). The ratio of the measured dielectric constants between the on- and off-states was close to ~10³ with slight
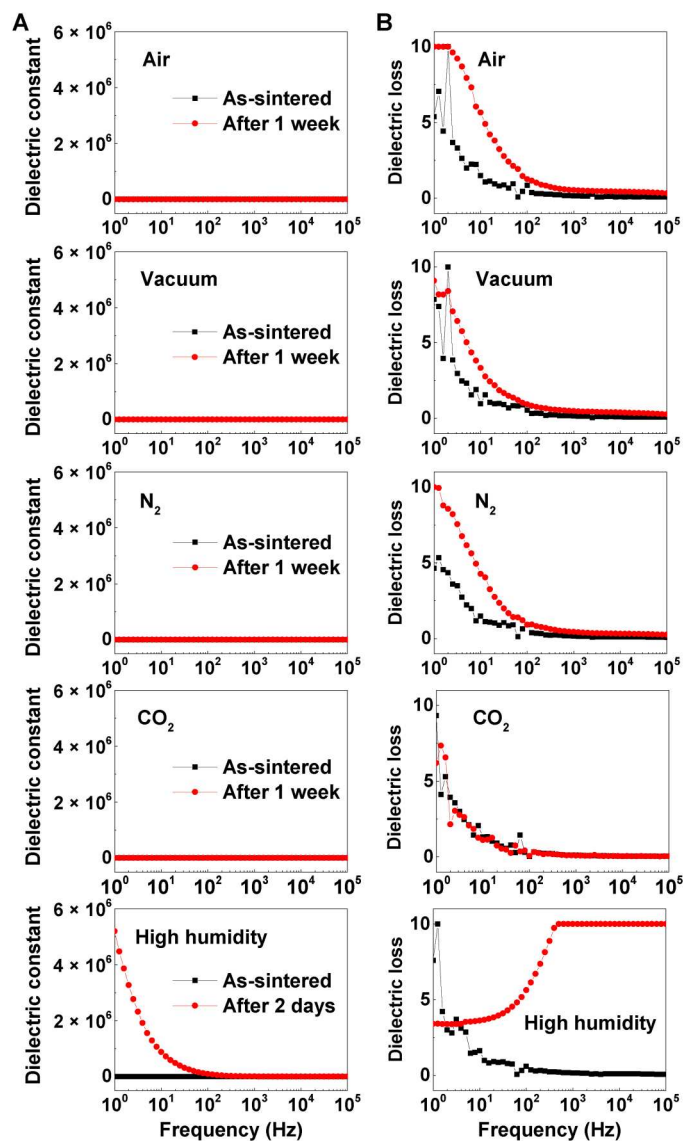
**Fig. 4. The evolution of dielectric responses in Ni-substituted BaTiO₃ ceramics under various ambient environments.** (**A**) Change of frequency-dependent dielectric constant in Ni-substituted BaTiO₃ ceramics under air, vacuum, nitrogen ($N_2$), carbon dioxide ($CO_2$), and high-humidity environments. (**B**) Corresponding dielectric loss in ceramics before and after chemical treatments.

variations throughout the whole cycles, indicating that the repetition of the dielectric on- and off-states was stably sustained.

To assess the humidity-sensing performance of our Ni-substituted BaTiO₃ ceramics systematically, we first prepared a ceramic capacitor with top/bottom Ag electrodes and monitored the evolution of electrical resistance in a humid condition, where relative humidity (RH) progressively increased from 0 to 80% in a stepwise manner with a time interval of about 1000 s (Fig. 6A). For a relative comparison, the air atmosphere was taken to RH = 0% as a reference condition. Unlike pure BaTiO₃, the Ni-substituted BaTiO₃ should incorporate a certain amount of oxygen vacancies resulting in electrical leakage and the linked dielectric loss (*42*, *46*). Owing to such a coupling between the electrical conductivity and the dielectric

property, we could evaluate a change in dielectric permittivity by examining the variation of electrical resistance depending on RH (*33*, *34*). As shown in Fig. 6B, it was clear that the resistance of Ni-substituted BaTiO₃ ceramics continuously decreased as soon as the degree of humidity increased step by step. When the humidity level was restored to the reference condition (RH = 0%), the corresponding resistance gradually went back to the initial value. By contrast, for pure BaTiO₃, a distinct change was not detected in the electrical resistance depending on the RH change (fig. S8). This indicated that the electrical and dielectric properties of our Ni-substituted BaTiO₃ were highly susceptible to moisture in air, which would be applicable to realize a humidity sensor with high sensitivity.

To get further insight on our observations [i.e., the emergence of two different dielectric states (off- and on-states) in substituted BaTiO₃ ceramics with 6H-hexagonal symmetry], we performed impedance analyses of the as-sintered (the off-state) and treated (the on-state attained by exposure to ambient air for 6 weeks) Ni-substituted BaTiO₃ ceramics. Note that our polycrystalline Ni-substituted BaTiO₃ ceramics with 6H-hexagonal symmetry included a large number of grains and grain boundaries, as depicted in Fig. 7A. To evaluate the capacitive and resistive contributions of the incorporated grains and grain boundaries separately, we harnessed a simple brick-layer model, where a polycrystalline ceramic was conceptually assumed to consist of indistinguishable cubic bricks (i.e., grains indicated by the hatched squares Fig. 7B) split by flat layers (i.e., grain boundaries indicated by the red solid lines in Fig. 7B) (*59*, *60*). When an external electric field (a black solid arrow in Fig. 7B) was applied to a system, two conducting channels were possible in the brick-layer model: (i) electrical currents (a blue dashed arrow in Fig. 7B) going through the horizontal grain boundaries only and (ii) electrical currents (a blue dash-dotted arrow in Fig. 7B) flowing through grains and vertical grain boundaries alternatively. Also, electrical circuits equivalent to these two current paths were also shown in Fig. 7C.

Two different impedance responses to external electric fields were clearly observed for the off- (the as-sintered state) and on-states (the treated state) of our Ni-substituted BaTiO₃ ceramics, as shown in Fig. 7 (D and E, respectively). In the impedance data of the as-sintered ceramics, an arc fitted to a single semicircle (the green solid curve) emerged for the off-state, whereas the corresponding Cole-Cole plots of the treated ceramics exhibited a curve deconvoluted to two semicircles (the red and green solid curves) with different sizes for the on-state. Such different impedance characteristics in the dielectric relaxation properties were also evident in the temperature-dependent Cole-Cole plots (figs. S9 and S10 for the off- and on-states, respectively). Note that each semicircular arc in a Cole-Cole plot represents dielectric relaxation arising from a parallel connection between one capacitor and one resistor (*61*, *62*). For the off-state, most of the electrical currents passed through one conducting channel (e.g., grain boundaries as the first case of the brick-layer model), and the resulting dielectric relaxation behavior followed a single-semicircular arc in the Cole-Cole plots of the as-sintered ceramics. In contrast, impedance signals from electrical currents passing through both grains and grain boundaries could induce the double-semicircular curve for the on-state (i.e., the treated ceramics), as aforementioned in the second case of the brick-layer model. This indicates that the pathway of electrical currents in Ni-substituted BaTiO₃ ceramics was modified, when the as-
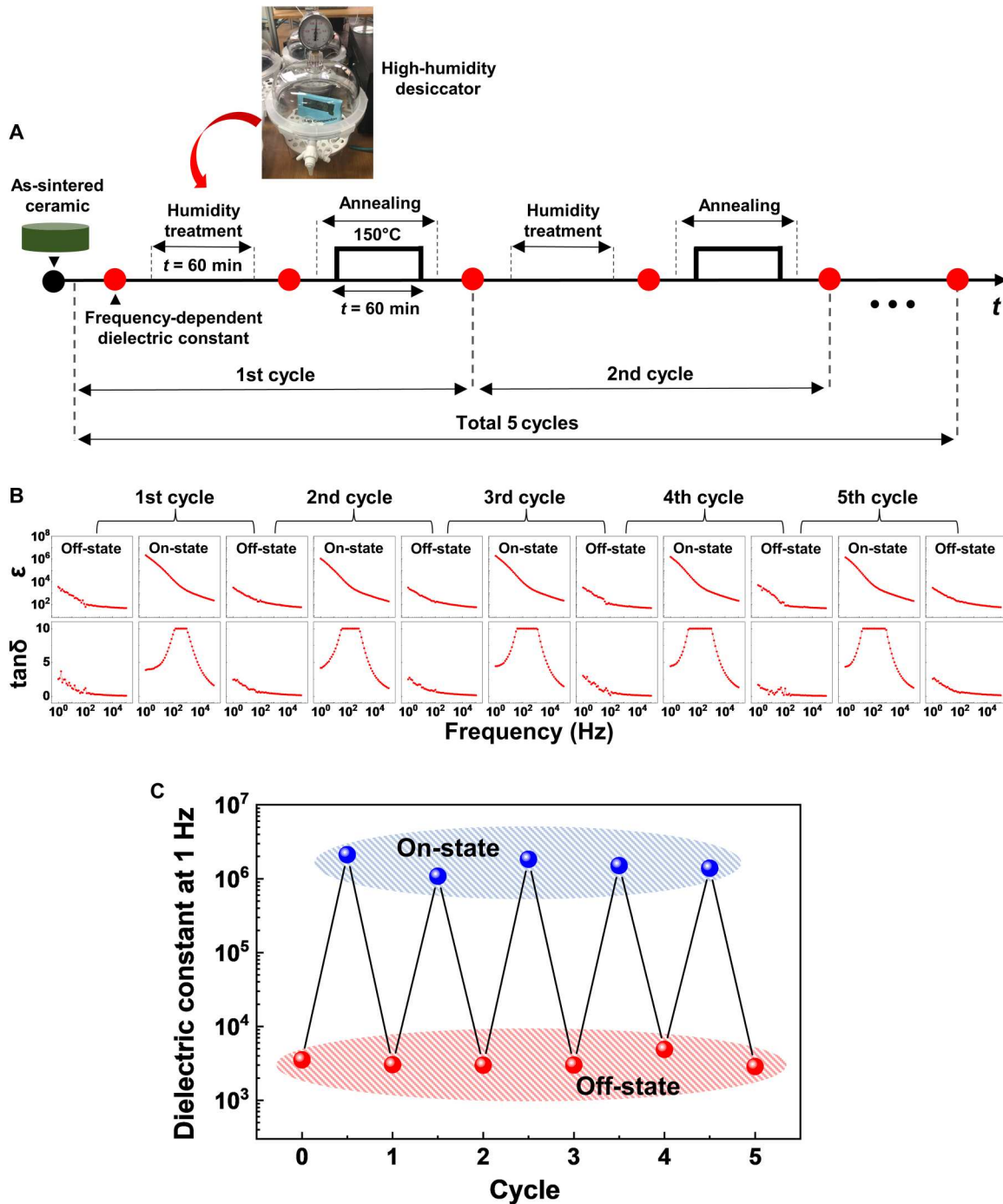
**Fig. 5. The reversible change of dielectric responses in Ni-substituted BaTiO₃ ceramics.** (**A**) The schematic of the experimental sequence to test recyclability of the dielectric on- and off-states. (**B**) The evolution of the frequency-dependent dielectric constant and loss of Ni-substituted BaTiO₃ ceramics under the repetitive cycles of a high-humidity treatment and thermal annealing. (**C**) The number of cycle dependence of dielectric constants at 1 Hz for the dielectric on- and off-states induced by the humidity treatment and the following thermal annealing, respectively. The red and blue circles represented the dielectric permittivity of ceramic samples after the thermal annealing (i.e., off-state) and after the treatment under a humid environment (i.e., on-state), respectively.
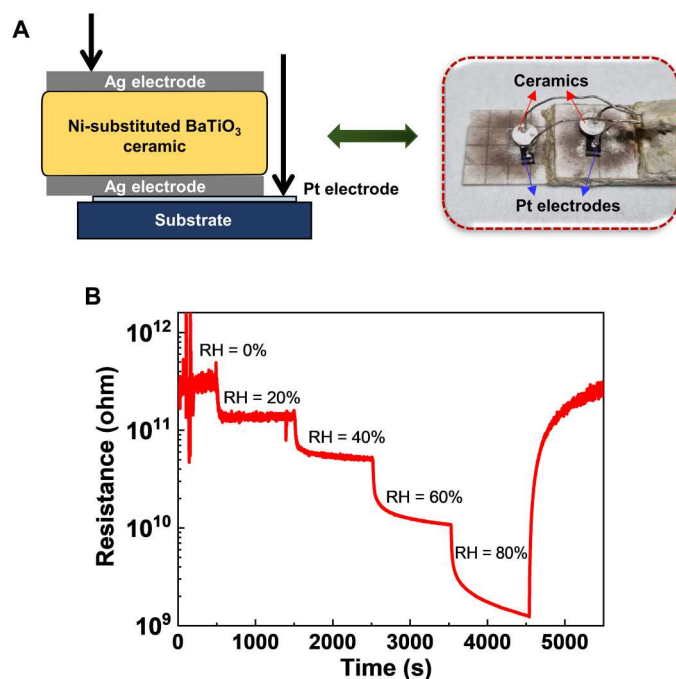
**Fig. 6. Sensing performance experiments.** (**A**) Schematic diagram of a humidity sensing experiment. (**B**) Resistive responses of Ni-substituted BaTiO$_3$ ceramics to the change in RH. A stepwise decrease in the electrical resistance of the sensors was observed with the increasing humidity levels. The electrical resistance of ceramics gradually recovered to the initial value when the RH changed from 80 to 0% again.

sintered ceramics were treated under the ambient air environment for 6 weeks.

To elucidate a microscopic origin of a discrepancy in dielectric responses between the off- and on-states, element-specific x-ray photoelectron spectroscopy (XPS) experiments were implemented for the as-sintered and treated Ni-substituted BaTiO$_3$ ceramics, as shown in Fig. 8 (A and B), respectively. Note that there was no distinct difference in the raw XPS spectra of Ba 3$d$, Ti 2$p$, and Ni 2$p$ bands, except for the O 1$s$ orbital (fig. S11). The raw O 1$s$ XPS data were deconvoluted to three different XPS spectra using the Gaussian-Lorentzian fitting (52, 63). The XPS peaks nearby binding energies of 529.1 (the red solid curve), 530.3 (the blue solid curve), and 531.2 eV (the black solid curve) were known to originate from lattice oxygens, oxygen vacancies, and chemisorbed oxygen ions, respectively (52, 64). The deconvoluted O 1$s$ XPS spectra revealed that the XPS peak attributed to chemisorbed oxygen species [e.g., hydroxyls (OH$^-$)] was strongly enhanced in the treated ceramics by exposure to ambient air for 4 weeks compared with the as-sintered ceramics. For other XPS peaks of lattice oxygens and oxygen vacancies, slight variations in the peak intensity were simply observed. It should be also noted that water molecules were involved with two different dielectric responses of the off- and on-states in Ni-substituted BaTiO$_3$ ceramics (Fig. 4 and fig. S7). Thus, it was plausible that water vapor (H$_2$O) in air was dissociated to a proton (H$^+$) and a hydroxyl (OH$^-$), and then the dissociated hydroxyl ions were adsorbed on the ceramic surface.

To evidence the existence of hydrogen ions in our Ni-substituted BaTiO$_3$ ceramics, time-of-flight secondary ion mass spectrometry (TOF-SIMS) measurements were performed for both pure and substituted ceramic samples. For a fair comparison, the pure and substituted BaTiO$_3$ ceramics at the as-sintered state were treated under the ambient environment for 6 weeks before TOF-SIMS experiments. For pure BaTiO$_3$ samples, the signals of hydrogen ions were simply collected on the surface of the ceramic specimens. In our TOF-SIMS data, the ceramic surface corresponded to the sputter time of 0 s in the three-dimensional (3D) rendering image visualizing the spatial distribution of H$^+$ ions (Fig. 8, C and D). Contrary to the pure BaTiO$_3$, the SIMS signals of hydrogen ions were extensively detected in the Ni-substituted BaTiO$_3$ throughout the whole volume of the ceramic sample. On the basis of our XPS results, it was highly likely that hydroxyl (OH$^-$) ions dissociated water molecules in air were adsorbed at oxygen vacancy sites on the surface of our Ni-substituted BaTiO$_3$ with noticeable oxygen off-stoichiometry. Because protons (H$^+$) are highly moveable because of the lightest ionic mass and the smallest ionic size (49), the separated hydrogen ions from water molecules would go into the treated Ni-substituted BaTiO$_3$ ceramics.

## DISCUSSION

We now discuss dc and ac resistivity of Ni-substituted BaTiO$_3$ ceramics for the as-sintered and treated states. The dc resistivity was calculated as follows

$$\rho_{dc} = R\frac{A}{d} \tag{2}$$

where $R$, $A$, and $d$ represented the electrical resistance, surface area, and thickness of ceramic pellets, respectively. On the basis of the electrical resistance data of the sensing experiments (Fig. 6B), the dc resistivity was estimated to ~8.6 × 10$^9$ ohms·m at a zero RH condition (RH = 0%), whereas it was ~4.1 × 10$^7$ ohms·m at a high RH condition (RH = 80%). On the other hand, we also extracted the ac resistivity ($\rho_{ac}$) from the measured dielectric constant ($\varepsilon$) and dielectric loss (tan$\delta$) using the following relation

$$\rho_{ac} = \frac{1}{2\pi f \varepsilon_0 \varepsilon \tan\delta} \tag{3}$$

where $\varepsilon_0$ was the permittivity of free space, and $f$ is the frequency of the applied voltage bias. At a frequency of 1 Hz, the ac resistivities were ~2.1 × 10$^6$ and 1.1 × 10$^3$ ohms·m for the as-sintered ceramic (i.e., off-state) and the treated ceramic by humidity (i.e., on-state), respectively (Fig. 4, bottom). Note that the ac resistivity ratio (~1.9 × 10$^3$) between off- and on-states was approximately an order of magnitude higher than the dc resistivity ratio (i.e., the proportion of the dc resistivity in a zero RH condition to that in a high RH condition ~2.1 × 10$^2$). It was highly likely that such a difference between the ac and dc resistivity ratios would be attributed to an interfacial effect between the Ag electrode and the ceramic sample (20). A further study would be highly desirable to elucidate the relationship between the ac and dc resistivities of the Ni-substituted BaTiO$_3$ ceramics.

Introduction of hydrogen ions dissociated from water molecules to Ni-substituted BaTiO$_3$ ceramics could produce two different dielectric properties in the low-frequency region, which were reversibly controllable via a treatment under a specific ambient environment and a reset process by external stimulation. The
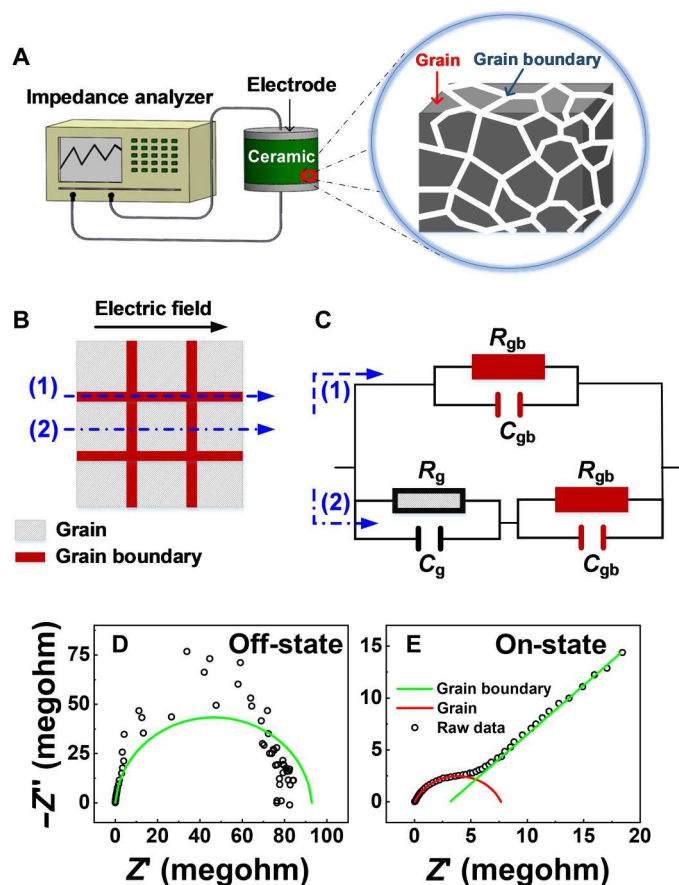
**Fig. 7. Impedance analyses of Ni-substituted BaTiO$_3$ ceramics at two dielectric states (i.e., off- and on-states). (A)** Experimental setup of impedance analysis. (**B**) Schematic diagram of a brick-layer model for a polycrystalline ceramic. (**C**) The equivalent electric circuit. The impedance complex plane plots in the Ni-substituted BaTiO$_3$ ceramics for the (**D**) off- and (**E**) on-states at room temperature.

energy-dispersive spectroscopy (EDS) analyses of the as-sintered ceramics showed that grain boundaries were more oxygen deficient than grains for the off-state exhibiting low dielectric permittivity at low frequencies (fig. S12). We stress that the measurement error of the oxygen element is around ~6% in the conventional EDS analyses (*65*). The difference in the atomic percentages of oxygen content between gains and grain boundaries (~25%) was still beyond the reported measurement accuracy (see fig. S13). It was therefore plausible that most oxygen vacancies were accumulated at grain boundaries in the as-sintered Ni-substituted BaTiO$_3$ ceramics initially (fig. S14A). In the as-sintered state (i.e., the off-state), the oxygen vacancy–rich grain boundaries would act as a conducting path of electrical currents, whereas the grains free from oxygen vacancies should be highly resistive. Such a difference in electrical conductance between grains and grain boundaries enabled electrical currents to pass through the grain boundaries largely, which was in agreement with our impedance results of the off-state (Fig. 7D). By contrast, when the as-sintered ceramics were exposed to ambient air for a long time (4 to 6 weeks), the polar hydroxyl (OH$^-$) ions dissociated from water molecules were adsorbed at oxygen vacancy sites nearby grain boundaries (fig. S14B). Meanwhile, the separated protons (H$^+$) from water molecules could move inside

grains (fig. S14C). In the presence of protons, grains became more conductive electrically in the treated Ni-substituted BaTiO$_3$ ceramics, and hence, the electrical current could pass through both the grains and the grain boundaries leading to double-semicircular curves in the dielectric relaxation behaviors of the on-state (Fig. 7E). In addition, in the presence of protons in the grains, the treated ceramics should be electrically leaky, resulting in an elliptical hysteresis curve (Figs. 2F and 3F) and an increase in dielectric loss (Fig. 4B). The electrical leakage in the treated Ni-substituted BaTiO$_3$ ceramics was also identified by local conducting atomic force microscopy (c-AFM) measurements (fig. S15). It was also worthwhile to discuss that the local electrical leakage in lossy dielectrics could affect the macroscopic dielectric responses with the increase of dielectric permittivity (*66*). On the other hand, as thermal stress was applied to the treated ceramic samples, the introduced hydrogen ions (H$^+$) could retreat with the desorption of hydroxyl ions (OH$^-$) to preserve charge neutrality (i.e., a reset process from the on-state to the initial off-state).

The conversion of the dielectric off-state to the dielectric on-state was also observed, when the as-sintered Ni-substituted BaTiO$_3$ ceramics remained under an ambient condition surrounding acetic acid (CH$_3$COOH) for 2 days (fig. S16). The measured dielectric constant in the frequency domain increased up to ~$2.0 \times 10^6$ at 1 Hz, and then the low-frequency dielectric permittivity rapidly decreased over time (fig. S17, A to C). Such a change in the dielectric responses induced by exposure to the acetic acid environment was only achievable in substituted BaTiO$_3$ ceramics with oxygen off-stoichiometry, not oxygen-rich pure BaTiO$_3$ (fig. S17, D to F). Considering that the acetic acid was a weak monoprotic acid donating a proton (H$^+$) easily (*67*), the modification of dielectric constants should be attributed to protonation of the oxygen-deficient BaTiO$_3$ ceramics.

It is important to discuss possible mechanisms of ultrahigh dielectric permittivity in the ambient environment–treated substituted BaTiO$_3$ ceramics. On the basis of previous literature, it was proposed that a transition to a relaxor ferroelectric phase accompanying a structural modification would induce dielectric anomalies in complex oxide ceramics (*68*). We emphasize that there was no structural difference between the as-sintered (the off-state) and treated (the on-state) Ni-substituted BaTiO$_3$ ceramics (fig. S18). According to the XRD results of our ceramic samples, their crystal structures were macroscopically 6H-hexagonal for both off- and on-states, regardless of a specific treatment under a humid environment. Thus, the low-frequency huge dielectric constant in the on-state would not be driven by a structural phase transition on a macroscopic scale.

Inhomogeneity in the structural and dielectric properties induced by protonation may be closely related to the colossal dielectric permittivity in Ni-substituted BaTiO$_3$ ceramics with 6H-hexagonal symmetry. For the off-state of our Ni-substituted BaTiO$_3$ ceramics, structural phases inside grains would rather be homogeneous with little variation in local dielectric permittivity, because most oxygen vacancies were accumulated nearby grain boundaries (figs. S12 to S14A). By contrast, for the on-state, a large amount of protons dissociated from the water molecules could be introduced into grains inducing heterogeneous distributions of the crystal structures and the electric polarizability microscopically (fig. S14C). At a lattice site containing a proton, the local crystal structure at an atomic level should be more deformed with the promoted
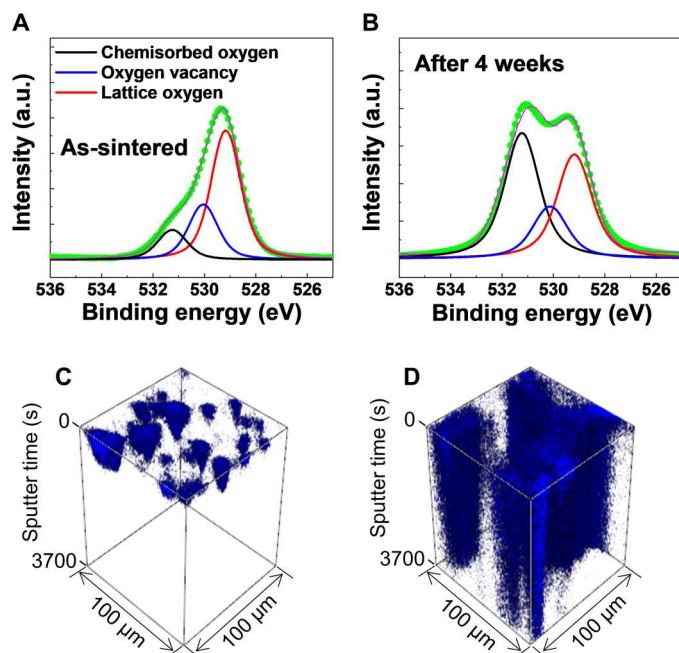
**Fig. 8. XPS and time-of-flight secondary ion mass spectrometry measurements.** XPS spectra at the O 1s edge of Ni-substituted BaTiO₃ ceramics (**A**) at the as-sintered state and (**B**) after 4 weeks in ambient air. The red, blue, and black solid lines in (A) and (B) represented the fitted curves of the oxygen in a lattice, the oxygen vacancy, and the chemisorbed oxygen on the surface of the ceramics. The volume fraction of the chemisorbed oxygen peak substantially increased after air exposure. Time-of-flight secondary ion mass spectrometry (TOF-SIMS) 3D rendering maps of $H^+$ signals in the (**C**) pure and (**D**) Ni-substituted BaTiO₃ ceramics that were treated by air exposure for 6 weeks (scale, 100 μm by 100 μm; sputter time, 0 to 3700 s).

electric polarizability (an increase of dielectric constant) by an internal field arising from the introduced proton (*40*, *41*). We stress that highly polarizable nano-domains with large dielectric constants could boost the electric polarizability of the neighboring nano-domains with small dielectric constants via a proximity effect (*69*, *70*). Thus, the inhomogeneity in the local dielectric responses by hydrogenation should produce a sizable enhancement of the overall dielectric permittivity in our Ni-substituted BaTiO₃ ceramics.

In summary, we demonstrated experimental manipulation of the frequency-dependent dielectric relaxation behaviors in complex oxide ceramics via designed treatments under specific ambient environments. Sizable enhancements of dielectric permittivity were clearly observed in the low-frequency domains, when the as-sintered Ni-substituted BaTiO₃ ceramics were exposed to water vapor–abundant conditions exhibiting high humidity. The low dielectric constant (~$10^3$ at 1 Hz) in the as-sintered state became three orders of magnitude higher (~$10^6$ at 1 Hz) compared with the treated state under humid circumstances. In addition, these two dielectric states (the low-frequency low and ultrahigh dielectric responses named as the off- and on-states, respectively) were reversibly controllable through external stimulation. We also identified that the off- and on-states of dielectric properties were involved with the adsorption of hydroxyl ions ($OH^-$) on surface oxygen vacancies and, meanwhile, the introduction of hydrogen

ions ($H^+$) through the water dissociation. The achieved huge dielectric permittivity in the ambient environment–treated Ni-substituted BaTiO₃ ceramics would originate from local differences in the crystal structures and the electric polarizability induced by the hydrogenation. Potentially, our results will be harnessed to realize high-performance oxide ceramic–based dielectric sensors (e.g., hygrometers), which are able to detect water vapor in ambient air with high efficiency and sensitivity.

## MATERIALS AND METHODS
### Sample preparation
The polycrystalline Ni-substituted BaTiO₃ ceramics [Ba(Ti$_{1−x}$Ni$_x$)O$_{3−δ}$] at doping concentrations (*x* = 0.175) were prepared by a conventional solid-state reaction method. High-purity BaCO₃, TiO₂, and NiO (99.9%, High Purity Chemicals, Saitama, Japan) were mixed in the molar ratio of 1:0.825:0.175, respectively and then calcinated at 1100°C for 8 hours in air for the chemical reaction. The calcined powders were reground, ball-milled again for 24 hours, and lastly dried to gain fine powders with much smaller grain size for pelletizing. After incorporating a few droplets of polyvinyl-alcohol {[CH₂CH(OH)] $_n$} binder solution with the interground powders, we molded a pellet of mixed powder with a diameter of 7 nm and then pelletized the pellet under a pressure of ~133 Pa. For crystallization, the Ni-substituted BaTiO₃ ceramic pellet was sintered in a box furnace at 1330°C for 6 hours in air. The densities of pure and Ni-substituted BaTiO₃ ceramics at the as-sintered state were 5.91 and 4.74 g/cm², respectively. This indicated that the Ni-substituted BaTiO₃ ceramics were less dense than the pure BaTiO₃ ceramics. The measured relative density of the Ni-substituted BaTiO₃ ceramics was ~82% of the theoretical density of the 6H-hexagonal BaTiO₃ phase (*71*). Considering that the relative density of porous BaTiO₃ with tetragonal symmetry was approximately 65% of the theoretical density of tetragonal BaTiO₃ (*72*, *73*), it was not likely that our Ni-substituted BaTiO₃ ceramics were porous.

### Structural characterization and transmission electron microscopy experiments
The crystalline structure of Ni-substituted BaTiO₃ ceramic samples was identified by an x-ray diffractometer with Cu Kα radiation at room temperature (*45*, *54*). Transmission electron microscopy samples of the Ni-substituted BaTiO₃ were prepared by the Ga ion beam milling method using a dual-beam focused ion beam system (Helios NanoLab 450, Thermo Fisher Scientific) and additionally milled by a low-energy Ar-ion milling system (Fishione Model 1040 Nanomill) to reduce damage at the surface layers of the samples. An aberration-corrected STEM (FEI Titan³ G2 60-300) system was used to obtain ABF STEM images of the samples with the detector angle range of 12 to 24 mrad. The probe convergence semi-angle and the source size of the electron probe were 26 mrad and 0.9 Å, respectively.

### Polarization electric field hysteresis and dielectric constant measurements
The ferroelectric polarization (*P-E*) loops were measured in a silicon oil bath using a modified Sawyer-Tower circuit with a high-voltage amplifier (TREK 610E). The temperature dependence of the dielectric constant of the samples was measured using an

impedance analyzer (HP4192A) over the temperature range from 30° to 350°C at the three different frequencies of $10^3$, $10^4$, and $10^5$ Hz. The frequency-dependent dielectric constant measurements were performed using a HIOKI 3522-50 analyzer at a frequency range from $10^0$ to $10^5$ Hz. Note that the impedance analyzer (HIOKI 3522-50) has a tanδ measuring range of 0.00001 to 9.99999.

## Impedance analyses

We analyzed the temperature-dependent impedance characteristics of our Ni-substituted BaTiO$_3$ ceramics for two different dielectric states (i.e., the off- and on-states). For the electrical impedance measurements, the top and bottom sides of the ceramic samples were coated with silver pastes, and then the specimens were cured in a box furnace at 700°C for 30 min. Ahead of the impedance analyses, the frequency-dependent dielectric permittivity of each sample was measured to check whether the ceramic compound remained in the off- and on-states. The impedance measurements were performed in the temperature range of 20° to 180°C using a HIOKI 3522-50 analyzer.

## Treatment of ceramics under various ambient environments

To examine the dielectric properties of our Ni-substituted BaTiO$_3$ ceramics, we deposited silver pastes on the top and bottom sides of as-sintered pellets and then annealed the silver-coated pellets at 700°C for 30 min for curing. Before a specific treatment under an ambient environment, we initially measured the frequency-dependent dielectric constant of ceramic capacitors at the as-sintered state. After the specific treatment of the ceramic samples, we remeasured their dielectric properties for comparison. We also monitored the evolution of dielectric responses of the Ni-substituted BaTiO$_3$ ceramics under various ambient conditions: (i) ambient air, (ii) vacuum and water vapor, (iii) N$_2$ and CO$_2$, (iv) liquid water, and (v) acetic acid. First, to examine the effect of ambient air on the dielectric responses of our Ni-substituted BaTiO$_3$ ceramics, we exposed the ceramic samples to the air environment at room temperature for the time duration of 6 weeks and then performed the dielectric permittivity measurement after the air exposure. Second, we treated the as-sintered Ni-substituted BaTiO$_3$ ceramics under vacuum and high-humidity environments. To investigate the dielectric characteristics of the ceramic samples in the vacuum state, the ceramics remained in the desiccator with a low vacuum pressure of 380 torr for 1 week. For an experiment under the humid atmosphere, we filled the plastic tray with deionized water and placed it on the bottom of the desiccator. Then, the ceramic specimens were placed above the water-filled tray to avoid a direct contact with liquid water. Last, we closed the desiccator and purged air inside it to adjust the internal pressure to 380 torr (see fig. S6 and table S2). Third, for ambient treatments under nitrogen (N$_2$) and carbon dioxide (CO$_2$) conditions, we put the as-sintered ceramics in the vacuum desiccator and evacuated the desiccator to a pressure of 380 torr. We inserted N$_2$ and CO$_2$ gas into the desiccator until the internal pressure reached ~700 torr. This procedure was repeated twice to provide a sufficient amount of N$_2$ and CO$_2$ gas into the desiccator (see fig. S6 and table S2). Fourth, for a treatment under a liquid water environment, the as-sintered Ni-substituted BaTiO$_3$ ceramics were immersed in deionized water for 10 min at room temperature. After the water treatment, the ceramic samples were dried under a circumstance of N$_2$ gas flow at room temperature.

Fifth, an experimental setup was constructed for a specific treatment under an acetic acid environment. In the beginning stage of this treatment, we poured acetic acid into a glass jar and put the as-sintered Ni-substituted BaTiO$_3$ ceramics into a beaker. The beaker with the ceramic samples was placed on the bottom of the jar to separate the ceramics from the acid liquid. Then, we closed the glass jar and the ceramic samples remained in the acetic acid–rich environment. After the time duration of 2 days, the ceramics were removed from the jar and dried under a circumstance of N$_2$ gas flow before dielectric measurements.

## The recyclability test of two dielectric states

In our Ni-substituted BaTiO$_3$ ceramics, we experimentally examined how stable the reversible change between two dielectric states (i.e., on- and off-states) was under the repeated cycle of a high-humidity treatment and thermal annealing. Initially, we measured the frequency-dependent dielectric responses of the as-sintered Ni-substituted BaTiO$_3$ ceramics (i.e., off-state). Next, the as-sintered ceramics were treated under a high-humidity environment for the time duration of 1 hour. After the humidity treatment, we remeasured the frequency-dependent dielectric permittivity and loss of the treated ceramics (i.e., on-state) to monitor changes in the dielectric properties. To recover the dielectric on-state to the off-state, the treated ceramics were thermally annealed at 150°C for 1 hour in a box furnace. Then, the frequency-dependent dielectric constant/loss measurements were followed over and over. The cycle of the high-humidity treatment and the thermal annealing was repeated five times to secure experimental reliability of the recyclability of the on- and off-states.

## XPS analyses

XPS measurements were conducted using a K-Alpha$^+$ XPS system (Thermo Fisher Scientific Inc., UK) equipped with a monochromated Al Kα x-ray source ($h\nu$ = 1486.6 eV) of spot size 400 μm, and charge compensation of the XPS samples was performed during analysis. The carbon C 1$s$ peak of hydrocarbon at a binding energy of 284.6 eV was used as a reference to take corrections of all the obtained spectra. A field-emission scanning electron microscope (JSM-7600, JEOL, Japan) with an EDS detector was used to visualize the surface morphology and analyze the chemical stoichiometry of our Ni-substituted BaTiO$_3$ ceramics.

## XAS measurements

XAS were measured in total electron yield mode at the 4D PES (photoemission spectroscopy) beamline in the Pohang accelerator laboratory. The signal was obtained by measuring the sample current generated by photon irradiation and normalized using an $I_0$ current measured by Au mesh in front of the samples to eliminate photon beam fluctuation.

## TOF-SIMS measurements

TOF-SIMS experiments were performed with a Hybrid SIMS (ION-TOF GmbH, Münster, Germany) in KBSI Busan Center by using a pulsed 30-keV Bi$_1$ primary beam with a current of 1.5 pA. The analyzed area used in this work is a square of 100 μm by 100 μm. Positive ion spectra were internally calibrated using H$^+$, H$_2^+$, CH$_3^+$, C$_2$H$_5^+$, and C$_3$H$_7^+$ peaks and normalized to the respective secondary total ion yields. The chemical images of the analyzed area are recorded with 128 × 128 pixel resolution during the data

acquisition. The depth profile is a square of 300 μm by 300 μm using a 1-keV cesium beam.

## Sensing performance experiments

The humidity sensing properties of ceramic samples (e.g., Ni-substituted BaTiO₃) were measured in a quartz tube (diameter, 3 cm; length, 30 cm) at room temperature. The RH levels (20 to 80 RH%) were calibrated by mixing the dry air with water vapor. Note that the humidity gas flow rate was 1000 sccm, which was controlled by a mass flow controller. The electrical conductivity of ceramic samples was measured by using a dc bias voltage of 0.5 V with a Keithley 2401 source meter, and all conductivity results were recorded by a homemade LabVIEW software.

## Supplementary Materials

**This PDF file includes:**
Supplementary Text
Figs. S1 to S18
Tables S1 to S3
References

## REFERENCES AND NOTES

1. J.-K. Huang, Y. Wan, J. Shi, J. Zhang, Z. Wang, W. Wang, N. Yang, Y. Liu, C.-H. Lin, X. Guan, L. Hu, Z.-L. Yang, B.-C. Huang, Y.-P. Chiu, J. Yang, V. Tung, D. Wang, K. Kalantar-Zadeh, T. Wu, X. Zu, L. Qiao, L.-J. Li, S. Li, High-κ perovskite membranes as insulators for two-dimensional transistors. *Nature* **605**, 262–267 (2022).

2. A. I. Kingon, J.-P. Maria, S. K. Streiffer, Alternative dielectrics to silicon dioxide for memory and logic devices. *Nature* **406**, 1032–1038 (2000).

3. S. Krohns, P. Lunkenheimer, S. Meissner, A. Reller, B. Gleich, A. Rathgeber, T. Gaugler, H. U. Buhl, D. C. Sinclair, A. Loidl, The route to resource-efficient novel materials. *Nat. Mater.* **10**, 899–901 (2011).

4. S. C. B. Mannsfeld, B. C. K. Tee, R. M. Stoltenberg, C. V. Chen, S. Barman, B. V. O. Muir, A. N. Sokolov, C. Reese, Z. Bao, Highly sensitive flexible pressure sensors with microstructured rubber dielectric layers. *Nat. Mater.* **9**, 859–864 (2010).

5. W. H. Ko, Q. Wang, Touch mode capacitive pressure sensors. *Sens. Actuator A Phys.* **75**, 242–251 (1999).

6. M. Acosta, N. Novak, V. Rojas, S. Patel, R. Vaish, J. Koruza, G. Rossetti Jr., J. Rödel, BaTiO₃-based piezoelectrics: Fundamentals, current status, and perspectives. *Appl. Phys. Rev.* **4**, 041305 (2017).

7. M. E. Lines, A. M. Glass, *Principles and Applications of Ferroelectrics and Related Materials* (Oxford Classic Text in the Physical Sciences, Oxford Univ. Press, 2001).

8. B. Jaffe, W. Cook, H. Jaffe, *Piezoelectric Ceramics* (Academic, 1971).

9. M. Dawber, K. M. Rabe, J. F. Scott, Physics of thin-film ferroelectric oxides. *Rev. Mod. Phys.* **77**, 1083–1130 (2005).

10. M. Arshad, H. Du, M. S. Javed, A. Maqsood, I. Ashraf, S. Hussain, W. Ma, H. Ran, Fabrication, structure, and frequency-dependent electrical and dielectric properties of Sr-doped BaTiO₃ ceramics. *Ceram. Int.* **46**, 2238–2246 (2020).

11. G. Wang, C. Wang, S. Huang, C. Lei, X. Sun, T. Li, L. Liu, Origin of colossal dielectric behavior in double perovskite Ba₂CoNbO₆. *J. Am. Ceram. Soc.* **96**, 2203–2210 (2013).

12. W. Z. Yang, M. S. Fu, X. Q. Liu, H. Y. Zhu, X. M. Chen, Giant dielectric response and mixed-valent structure in the layered-ordered double-perovskite ceramics. *Ceram. Int.* **37**, 2747–2753 (2011).

13. W. Hu, Y. Liu, R. L. Withers, T. J. Frankcombe, L. Norén, A. Snashall, M. Kitchin, P. Smith, B. Gong, H. Chen, S. Jason, F. Brink, J. Wong-Leung, Electron-pinned defect-dipoles for high-performance colossal permittivity materials. *Nat. Mater.* **12**, 821–826 (2013).

14. Y. Song, X. Wang, Y. Sui, Z. Liu, Y. Zhang, H. Zhan, B. Song, Z. Liu, Z. Lv, L. Tao, J. Tang, Origin of colossal dielectric permittivity of rutile Ti₀.₉In₀.₀₅Nb₀.₀₅O₂: Single crystal and polycrystalline. *Sci. Rep.* **6**, 21478 (2016).

15. H. Han, C. Voisin, S. Guillemet-Fritsch, P. Dufour, C. Tenailleau, C. Turner, J. C. Nino, Origin of colossal permittivity in BaTiO₃ via broadband dielectric spectroscopy. *J. Appl. Phys.* **113**, 024102 (2013).

16. S. Guillemet-Fritsch, Z. Valdez-Nava, C. Tenailleau, T. Lebey, B. Durand, J.-Y. Chane-Ching, Colossal permittivity in ultrafine grain size BaTiO₃₋ₓ and Ba₀.₉₅La₀.₀₅TiO₃₋ₓ materials. *Adv. Mater.* **20**, 551–555 (2008).

17. C. C. Homes, T. Vogt, S. M. Shapiro, S. Wakimoto, A. P. Ramirez, Optical response of high-dielectric-constant perovskite-related oxide. *Science* **293**, 673–676 (2001).

18. M. A. Subramanian, D. Li, N. Duan, B. A. Reisner, A. W. Sleight, High dielectric constant in ACu₃Ti₄O₁₂ and ACu₃Ti₃FeO₁₂ phases. *J. Solid State Chem.* **151**, 323–325 (2000).

19. A. P. Ramirez, M. A. Subramanian, M. Gardel, G. Blumberg, D. Li, T. Vogt, S. M. Shapiro, Giant dielectric constant response in a copper-titanate. *Solid State Commun.* **115**, 217–220 (2000).

20. P. Lunkenheimer, R. Fichtl, S. G. Ebbinghaus, A. Loidl, Nonintrinsic origin of the colossal dielectric constants inCaCu₃Ti4O₁₂. *Phys. Rev. B* **70**, 172102 (2004).

21. P. Lunkenheimer, V. Bobnar, A. V. Pronin, A. I. Ritus, A. A. Volkov, A. Loidl, Origin of apparent colossal dielectric constants. *Phys. Rev. B* **66**, 052105 (2002).

22. D. C. Sinclair, T. B. Adams, F. D. Morrison, A. R. West, CaCu₃Ti₄O₁₂: One-step internal barrier layer capacitor. *Appl. Phys. Lett.* **80**, 2153–2155 (2002).

23. M. Li, X. L. Chen, D. F. Zhang, W. Y. Wang, W. J. Wang, Humidity sensitive properties of pure and Mg-doped CaCu₃Ti₄O₁₂. *Sens. Actuators B Chem.* **147**, 447–452 (2010).

24. B. M. Kulwicki, Humidity sensors. *J. Am. Ceram. Soc.* **74**, 697–708 (1991).

25. S. Wan, H. Bi, Y. Zhou, X. Xie, S. Su, K. Yin, L. Sun, Graphene oxide as high-performance dielectric materials for capacitive pressure sensors. *Carbon* **114**, 209–216 (2017).

26. X. Liu, S. Cheng, H. Liu, S. Hu, D. Zhang, H. Ning, A survey on gas sensing technology. *Sensors* **12**, 9635–9665 (2012).

27. A. Dey, Semiconductor metal oxide gas sensors: A review. *Mater. Sci. Eng. B* **229**, 206–217 (2018).

28. P. M. Harrey, B. J. Ramsey, P. S. A. Evans, D. J. Harrison, Capacitive-type humidity sensors fabricated using the offset lithographic printing process. *Sens. Actuators B Chem.* **87**, 226–232 (2002).

29. T. Ishihara, S. Matsubara, Capacitive type gas sensors. *J. Electroceramics* **2**, 215–228 (1998).

30. W. C. Wang, Y. T. Tian, K. Li, E. Y. Lu, D. S. Gong, X. J. Li, Capacitive humidity-sensing properties of Zn₂SiO₄ film grown on silicon nanoporous pillar array. *Appl. Surf. Sci.* **273**, 372–376 (2013).

31. P. Bindra, A. Hazra, Selective detection of organic vapors using TiO₂ nanotubes based single sensor at room temperature. *Sens. Actuators B Chem.* **290**, 684–690 (2019).

32. H. Bi, K. Yin, X. Xie, J. Ji, S. Wan, L. Sun, M. Terrones, M. S. Dresselhaus, Ultrahigh humidity sensitivity of graphene oxide. *Sci. Rep.* **3**, 2714 (2013).

33. D. M. Pozar, *Microwave Engineering* (Wiley, 2011).

34. K. C. Kao, *Dielectric Phenomena in Solids* (Elsevier, 2004).

35. H. Yoon, M. Choi, T.-W. Lim, H. Kwon, K. Ihm, J. K. Kim, S.-Y. Choi, J. Son, Reversible phase modulation and hydrogen storage in multivalent VO₂ epitaxial thin films. *Nat. Mater.* **15**, 1113–1119 (2016).

36. A. Janotti, C. G. Van de Walle, Hydrogen multicentre bonds. *Nat. Mater.* **6**, 44–47 (2007).

37. S. Shen, Z. Li, Z. Tian, W. Luo, S. Okamoto, P. Yu, Emergent Ferromagnetism with Fermi-Liquid Behavior in Proton IntercalatedCaRuO₃. *Phys. Rev. X* **11**, 021018 (2021).

38. R. D. Shannon, Revised effective ionic radii and systematic studies of interatomic distances in halides and chalcogenides. *Acta Crystallogr. A* **32**, 751–767 (1976).

39. C. Amsler, M. Doser, M. Antonelli, D. M. Asner, K. S. Babu, H. Baer, H. R. Band, R. M. Barnett, E. Bergren, J. Beringer, G. Bernardi, W. Bertl, H. Bichsel, O. Biebel, P. Bloch, E. Blucher, S. Blusk, R. N. Cahn, M. Carena, C. C. A. Ceccucci, D. Chakraborty, M. C. Chen, R. S. Chivukula, G. Cowan, O. Dahl, G. D'Ambrosio, T. Damour, A. de Gouvêa, T. DeGrand, B. Dobrescu, M. Drees, D. A. Edwards, S. Eidelman, V. D. Elvira, V. V. Ezhela, J. L. Feng, W. Fetscher, B. D. Fields, B. Foster, T. K. Gaisser, L. Garren, H. J. Gerber, G. Gerbier, T. Gherghetta, G. F. Giudice, M. Goodman, C. Grab, A. V. Gritsan, J. F. Grivaz, Review of particle physics. *Phys. Lett. B* **667**, 1–6 (2008).

40. C. H. Park, D. J. Chadi, Effect of interstitial hydrogen impurities on ferroelectric polarization in PbTiO₃. *Phys. Rev. Lett.* **84**, 4717–4720 (2000).

41. H. Lee, T. H. Kim, J. J. Patzner, H. Lu, J.-W. Lee, H. Zhou, W. Chang, M. K. Mahanthappa, E. Y. Tsymbal, A. Gruverman, C.-B. Eom, Imprint control of BaTiO₃ thin films via chemically induced surface polarization pinning. *Nano Lett.* **16**, 2400–2406 (2016).

42. D. C. Sinclair, J. M. S. Skakle, F. D. Morrison, R. I. Smith, T. P. Beales, Structure and electrical properties of oxygen-deficient hexagonal BaTiO₃. *J. Mater. Chem.* **9**, 1327–1331 (1999).

43. R. D. Burbank, H. T. Evans, The crystal structure of hexagonal barium titanate. *Acta Crystallogr.* **1**, 330–336 (1948).

44. H. T. Langhammer, T. Müller, K. H. Felgner, H. P. Abicht, Crystal structure and related properties of manganese-doped barium titanate ceramics. *J. Am. Ceram. Soc.* **83**, 605–611 (2000).

45. N. X. Duong, J.-S. Bae, J. Jeon, S. Y. Lim, S. H. Oh, A. Ullah, M. Sheeraz, J. San Choi, J.-H. Ko, S. M. Yang, K.-H. Kim, I. W. Kim, C. W. Ahn, T. H. Kim, Polymorphic phase transition in BaTiO₃ by Ni doping. *Ceram. Int.* **45**, 16305–16310 (2019).

46. G. M. Keith, M. J. Rampling, K. Sarma, N. M. Alford, D. C. Sinclair, Synthesis and characterisation of doped 6H-BaTiO₃ ceramics. *J. Eur. Ceram. Soc.* **24**, 1721–1724 (2004).

47. R. E. Cohen, Origin of ferroelectricity in perovskite oxides. *Nature* **358**, 136–138 (1992).

48. R. Schaub, P. Thostrup, N. Lopez, E. Lægsgaard, I. Stensgaard, J. K. Nørskov, F. Besenbacher, Oxygen vacancies as active sites for water dissociation on rutile $TiO_2$ (110). *Phys. Rev. Lett.* **87**, 266104 (2001).

49. K. D. Kreuer, Aspects of the formation and mobility of protonic charge carriers and the stability of perovskite-type oxides. *Solid State Ion.* **125**, 285–302 (1999).

50. A. Hanada, K. Kinoshita, S. Kishida, Resistive switching by migration of hydrogen ions. *Appl. Phys. Lett.* **101**, 043507 (2012).

51. H. Han, C. Davis III, J. C. Nino, Variable range hopping conduction in $BaTiO_3$ ceramics exhibiting colossal permittivity. *J. Phys. Chem. C* **118**, 9137–9142 (2014).

52. G. Panchal, D. K. Shukla, R. J. Choudhary, V. R. Reddy, D. M. Phase, The effect of oxygen stoichiometry at the interface of epitaxial $BaTiO_3/La_{0.7}Sr_{0.3}MnO_3$ bilayers on its electronic and magnetic properties. *J. Appl. Phys.* **122**, 085310 (2017).

53. S. Majumder, P. Basera, M. Tripathi, R. J. Choudhary, S. Bhattacharya, K. Bapna, D. M. Phase, Elucidating the origin of magnetic ordering in ferroelectric $BaTiO_{3-\delta}$ thin film via electronic structure modification. *J. Phys. Condens. Matter* **31**, 205001 (2019).

54. M. Sheeraz, M. U. Rashid, A. Ali, F. Akram, H. J. Lee, J. San Choi, J.-S. Bae, Y. S. Kim, Y.-H. Shin, C. W. Ahn, T. H. Kim, Stabilization of 6H-hexagonal $SrMnO_3$ polymorph by $Al_2O_3$ insertion. *J. Eur. Ceram. Soc.* **41**, 5155–5162 (2021).

55. R. Yimnirun, J. Tangsritrakul, S. Rujirawat, S. Limpijumnong, Identification of Mn site in $BaTiO_3$ by synchrotron X-ray absorption spectroscopy measurements. *Ferroelectrics* **381**, 130–143 (2009).

56. J. F. Scott, Ferroelectrics go bananas. *J. Phys. Condens. Matter* **20**, 021001 (2007).

57. K. Parida, S. Das, P. K. Mahapatra, R. N. P. Choudhary, Relaxor behavior and impedance spectroscopic studies of chemically synthesized $SrCu_3Ti_4O_{12}$ ceramic. *Mater. Res. Bull.* **111**, 7–16 (2019).

58. W. Q. Cao, L. F. Xu, M. M. Ismail, L. L. Huang, Colossal dielectric constant of $NaNbO_3$ doped $BaTiO_3$ ceramics. *Mater. Sci. Poland* **34**, 322–329 (2016).

59. N. M. Beekmans, L. Heyne, Correlation between impedance, microstructure and composition of calcia-stabilized zirconia. *Electrochim. Acta* **21**, 303–310 (1976).

60. H. Näfe, Ionic conductivity of $ThO_2$- and $ZrO_2$-based electrolytes between 300 and 2000 K. *Solid State Ion.* **13**, 255–263 (1984).

61. J. R. Macdonald, E. Barsoukov, *Impedance Spectroscopy: Theory, Experiment, and Applications* (Wiley, 2005).

62. D. C. Sinclair, A. R. West, Impedance and modulus spectroscopy of semiconducting $BaTiO_3$ showing positive temperature coefficient of resistance. *J. Appl. Phys.* **66**, 3850–3856 (1989).

63. J. S. Choi, C. W. Ahn, J.-S. Bae, T. H. Kim, Identifying a perovskite phase in rare-earth nickelates using X-ray photoelectron spectroscopy. *Curr. Appl. Phys.* **20**, 102–105 (2020).

64. C. Miot, E. Husson, C. Proust, R. Erre, J. P. Coutures, X-ray photoelectron spectroscopy characterization of barium titanate ceramics prepared by the citric route. Residual carbon study. *J. Mater. Res.* **12**, 2388–2392 (1997).

65. D. E. Newbury, N. Ritchie, Electron-excited x-ray microanalysis at low beam energy: Almost always an adventure! *Microsc. Microanal.* **22**, 735–753 (2016).

66. A. C. Caballero, M. Villegas, J. F. Fernandez, M. Viviani, M. T. Buscaglia, M. Leoni, Effect of humidity on the electrical response of porous $BaTiO_3$ ceramics. *J. Mater. Sci. Lett.* **18**, 1297–1299 (1999).

67. R. N. Goldberg, N. Kishore, R. M. Lennen, Thermodynamic quantities for the ionization reactions of buffers. *J. Phys. Chem. Ref. Data* **31**, 231–370 (2002).

68. E. Sun, W. Cao, Relaxor-based ferroelectric single crystals: Growth, domain engineering, characterization and applications. *Prog. Mater. Sci.* **65**, 124–210 (2014).

69. F. Li, S. Zhang, D. Damjanovic, L. Q. Chen, T. R. Shrout, Local structural heterogeneity and electromechanical responses of ferroelectrics: Learning from relaxor ferroelectrics. *Adv. Funct. Mater.* **28**, 1801504 (2018).

70. N. Qu, H. Du, X. Hao, A new strategy to realize high comprehensive energy storage properties in lead-free bulk ceramics. *J. Mater. Chem. C* **7**, 7993–8002 (2019).

71. R. M. Glaister, H. F. Kay, An investigation of the cubic-hexagonal transition in barium titanate. *Proc. Phys. Soc.* **76**, 763–771 (1960).

72. S. M. Gaytan, M. A. Cadena, H. Karim, D. Delfin, Y. Lin, D. Espalin, E. MacDonald, R. B. Wicker, Fabrication of barium titanate by binder jetting additive manufacturing technology. *Ceram. Int.* **41**, 6610–6619 (2015).

73. H. Kim, A. Renteria-Marquez, M. D. Islam, L. A. Chavez, C. A. Garcia Rosales, M. A. Ahsan, T. L. B. Tseng, N. D. Love, Y. Lin, Fabrication of bulk piezoelectric and dielectric $BaTiO_3$ ceramics using paste extrusion 3D printing technique. *J. Am. Ceram. Soc.* **102**, 3685–3694 (2019).

74. G. Panchal, R. J. Choudhary, S. Yadav, D. M. Phase, Probing the effect of ferroelectric to paraelectric phase transition on the Ti-3*d* and O-2*p* hybridization in $BaTiO_3$. *J. Appl. Phys.* **125**, 214102 (2019).

75. L. Ni, M. Fu, X. Ren, Y. Zhang, Enhanced dielectric relaxations in spark plasma sintered $CaCu_3Ti_4O_{12}$ ceramics. *J. Mater. Sci. Mater. Electron.* **28**, 10191–10198 (2017).

76. Y. Wu, X. Zhao, J. Zhang, W. Su, J. Liu, Huge low-frequency dielectric response of (Nb, In)-doped $TiO_2$ ceramics. *Appl. Phys. Lett.* **107**, 242904 (2015).

77. Y. Song, P. Liu, W. Wu, Q. Zhou, High-performance colossal permittivity for textured (Al + Nb) co-doped $TiO_2$ ceramics sintered in nitrogen atmosphere. *J. Eur. Ceram. Soc.* **41**, 4146–4152 (2021).

78. S. Kim, H. J. Avila-Paredes, S. Wang, C.-T. Chen, R. A. De Souza, M. Martin, Z. A. Munir, On the conduction pathway for protons in nanocrystalline yttria-stabilized zirconia. *Phys. Chem. Chem. Phys.* **11**, 3035–3038 (2009).